Article

Developmental Cell

An Organized Co-assembly of Clathrin Adaptors Is Essential for Endocytosis

Graphical Abstract

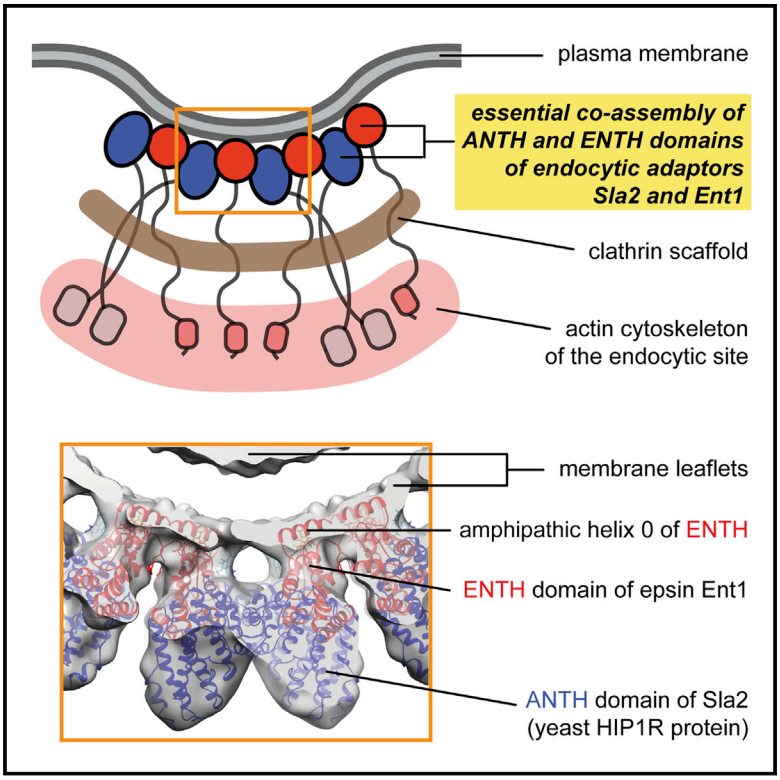

Authors

Michal Skruzny, Ambroise Desfosses, ..., Carsten Sachse, Marko Kaksonen

Correspondence

carsten.sachse@embl.de (C.S.), kaksonen@embl.de (M.K.)

In Brief

Clathrin-mediated endocytosis is the main plasma-membrane-to-cytoplasm vesicle trafficking route. Skruzny et al. shed light on the structural role of clathrin adaptors, showing that yeast clathrin adaptors Sla2 and Ent1 (homologs of mammalian Hip1r and epsin) form a regular, membrane-bound co-assembly essential for endocytic vesicle formation.

Highlights

- ANTH and ENTH domains of clathrin adaptors Sla2 and Ent1 form lattices on membranes
- Membrane-binding ANTH and ENTH domains oligomerize in a PI(4,5)P_2-dependent manner
- Cryo-EM showed a staggered arrangement of the ANTH-ENTH lattice on the membrane
- Regular co-assembly of clathrin adaptors Sla2 and Ent1 is essential for endocytosis

Accession Numbers

5avh

Skruzny et al., 2015, Developmental Cell *33*, 150–162
April 20, 2015
http://dx.doi.org/10.1016/j.devcel.2015.02.023

CellPress

Developmental Cell
Article

An Organized Co-assembly of Clathrin Adaptors Is Essential for Endocytosis

Michal Skruzny,[1,5,7] Ambroise Desfosses,[1,2,6,7] Simone Prinz,[2] Svetlana O. Dodonova,[2] Anna Gieras,[3] Charlotte Uetrecht,[4] Arjen J. Jakobi,[2,3] Marc Abella,[1] Wim J.H. Hagen,[2] Joachim Schulz,[4] Rob Meijers,[3] Vladimir Rybin,[2] John A.G. Briggs,[1,2] Carsten Sachse,[2,*] and Marko Kaksonen[1,2,*]

[1]Cell Biology and Biophysics Unit, European Molecular Biology Laboratory (EMBL), 69117 Heidelberg, Germany
[2]Structural and Computational Biology Unit, EMBL, 69117 Heidelberg, Germany
[3]EMBL Hamburg Unit, EMBL, 22607 Hamburg, Germany
[4]WP-79 Sample Environment Group, European XFEL GmbH, 22607 Hamburg, Germany
[5]Present address: Max Planck Institute for Terrestrial Microbiology and LOEWE Center for Synthetic Microbiology (SYNMIKRO), 35043 Marburg, Germany
[6]Present address: School of Biological Sciences, The University of Auckland, 1010 Auckland, New Zealand
[7]Co-first author
*Correspondence: carsten.sachse@embl.de (C.S.), kaksonen@embl.de (M.K.)
http://dx.doi.org/10.1016/j.devcel.2015.02.023

SUMMARY

Clathrin-mediated endocytosis, the main trafficking route from the plasma membrane to the cytoplasm, is critical to many fundamental cellular processes. Clathrin, coupled to the membrane by adaptor proteins, is thought to play a major structural role in endocytosis by self-assembling into a cage-like lattice around the forming vesicle. Although clathrin adaptors are essential for endocytosis, little is known about their structural role in this process. Here we show that the membrane-binding domains of two conserved clathrin adaptors, Sla2 and Ent1, co-assemble in a PI(4,5)P_2-dependent manner to form organized lattices on membranes. We determined the structure of the co-assembled lattice by electron cryo-microscopy and designed mutations that specifically impair the lattice formation in vitro. We show that these mutations block endocytosis in vivo. We suggest that clathrin adaptors not only link the polymerized clathrin to the membrane but also form an oligomeric structure, which is essential for membrane remodeling during endocytosis.

INTRODUCTION

Clathrin-mediated endocytosis is a key cellular trafficking pathway responsible for the uptake of many hormones and nutrients, retrieval of synaptic vesicle proteins after neurotransmission and the up-/downregulation of several signaling pathways (McMahon and Boucrot, 2011). During endocytosis, a small region of plasma membrane gets reshaped from an initially flat membrane to a closed vesicle by the concerted action of multiple endocytic proteins. The remodeling of the membrane requires mechanical force. Several mechanisms of membrane remodeling have been proposed and specific endocytic proteins have been suggested to be involved in membrane reshaping (Kozlov et al., 2014). However, the contributions and interplay of individual remodeling mechanisms to endocytic vesicle formation are only beginning to be understood.

An important role in shaping the forming vesicle has traditionally been attributed to the polymerized clathrin scaffold. To assemble at the endocytic site clathrin requires adaptor proteins that link clathrin to the plasma membrane by their clathrin-interaction motifs and membrane-binding domains. Although several clathrin adaptors including epsin and BAR-domain-containing proteins have been shown to have their own membrane remodeling activities (Boucrot et al., 2012, Henne et al., 2010; Mim and Unger, 2012), the clathrin scaffold is thought to be critical for their localization, concentration, and eventual organization (Kirchhausen et al., 2014).

Local polymerization of actin filaments is another important mechanism to drive membrane invagination especially when an extra force is needed to overcome a high turgor pressure or membrane tension of the cell (Aghamohammadzadeh and Ayscough, 2009; Basu et al., 2014; Boulant et al., 2011). Interestingly, the coupling of the polymerizing actin cytoskeleton to the membrane also requires clathrin adaptors. In this case, a conserved pair of clathrin adaptors Sla2 and Ent1 (Hip1r and epsin in mammals) links actin to the plasma membrane by their actin- and membrane-binding domains (Messa et al., 2014; Skruzny et al., 2012).

In addition to endocytic proteins, the specific plasma membrane lipid phosphatidylinositol 4,5-bisphospate (PI(4,5)P_2) is crucial for endocytic membrane reshaping. PI(4,5)P_2 is selectively enriched at endocytic sites, where it binds to the membrane-binding domains of many clathrin adaptors. Depletion of PI(4,5)P_2 from the membrane was shown to block early stages of endocytosis, probably before membrane invagination begins (Sun and Drubin, 2012; Zoncu et al., 2007).

Taken together, it is clear that clathrin adaptors are key factors in membrane reshaping during endocytosis. All described remodeling mechanisms (clathrin scaffolding, actin polymerization, an amphipathic helix insertion or scaffolding by clathrin adaptors) rely on clathrin adaptors to transmit bending forces to the plasma membrane. Although the structural details of the interactions between adaptors and clathrin, actin, or membrane

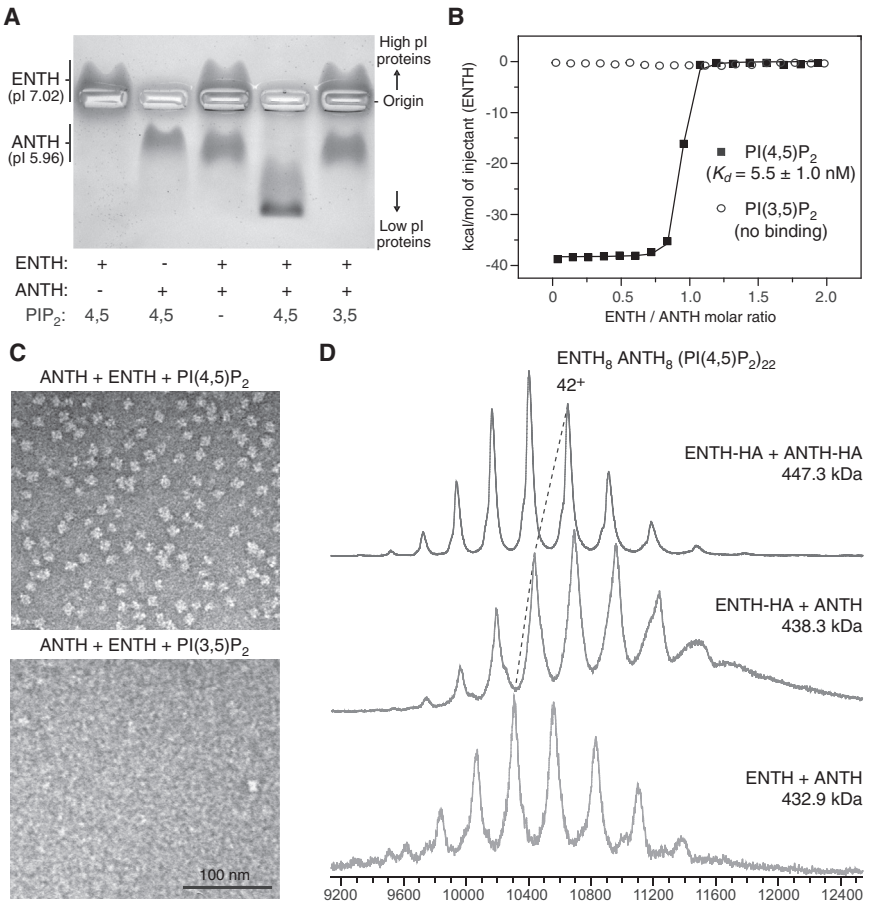

Figure 1. Sla2 ANTH and Ent1 ENTH Membrane-Binding Domains Oligomerize in PI(4,5)P_2-Dependent Manner In Vitro

(A) Native agarose gel electrophoresis (pH 7.0) of indicated combinations of proteins and soluble diC8-PIP_2 lipids.

(B) Isothermal titration calorimetry (ITC) of ANTH-ENTH interaction in the presence of indicated diC8-PIP_2 lipids.

(C) Electron micrographs of negatively stained diC8-PI(4,5)P_2-dependent ANTH-ENTH oligomeric complex.

(D) The stoichiometry of ANTH-ENTH-diC8-PI(4,5)P_2 oligomeric complex analyzed by native mass spectrometry at acceleration voltages of 100 V. Masses as determined from displayed spectra (SD = 0.1 kDa). The dashed line connects peaks carrying 42 charges. Extra charges on surface-exposed ANTH-HA-tags likely shift the charge state distribution of ANTH-HA+ENTH-HA to lower *m/z*.

See also Figure S1.

have been described (Brett et al., 2006; Kirchhausen et al., 2014; Owen et al., 2004), no structural organization of the adaptors at the endocytic site has previously been suggested.

Here we describe the structural role of two important clathrin adaptors Sla2 and Ent1 at the endocytic site. We show that the membrane-binding domains of Sla2 and Ent1 form a regular co-assembly on PI(4,5)P_2-containing membranes. Using electron cryo-microscopy, we resolved the structure of this co-assembly and show that it is essential for endocytosis. We propose that the co-assembly of Sla2 and Ent1 adaptors is critical for transmitting the membrane-remodeling forces during endocytosis.

RESULTS

Sla2 ANTH and Ent1 ENTH Membrane-Binding Domains Oligomerize in a PI(4,5)P_2-Dependent Manner In Vitro

In search of functionally important interactions of clathrin adaptors, we focused on the evolutionarily conserved interaction between the membrane-binding domains of yeast clathrin adaptors Sla2 and Ent1. The interaction between the ANTH domain of Sla2 and the ENTH domain of Ent1 was initially identified by an in vitro pull-down assay in the presence of a soluble form of their specific lipid ligand diC8-PI(4,5)P_2 (Skruzny et al., 2012) and recently also shown for the homologous mammalian proteins Hip1r and epsin 1 (Messa et al., 2014).

We first analyzed the thermodynamics of the ANTH-ENTH interaction and its dependency on PI(4,5)P_2. By native gel electrophoresis we found that Sla2's ANTH and Ent1's ENTH domains formed a complex specifically upon addition of diC8-PI(4,5)P_2, but not upon addition of diC8-PI(3,5)P_2 (Figure 1A). We then determined the K_d of the ANTH-ENTH interaction in the presence of diC8-PI(4,5)P_2 using isothermal titration calorimetry (ITC) (Figures 1B and S1A). We measured the K_d for this interaction to be 5.5 nM. This K_d is very low in comparison to known K_d values for interactions of clathrin adaptors, which are typically in micromolar range (Owen et al., 2004). The low K_d value together with a significant value of enthalpy for the ANTH-ENTH interaction (−38.3 kcal/mol) indicated that the ANTH and ENTH domains might oligomerize. To assess this possibility, we mixed both domains with diC8-PI(4,5)P_2 or diC8-PI(3,5)P_2 and analyzed these samples by electron microscopy using negative staining. We observed large regular particles of 18 nm in diameter specifically in the ANTH-ENTH-diC8-PI(4,5)P_2 sample (Figure 1C), suggesting that ANTH and ENTH domains form regular supramolecular assemblies in the presence of diC8-PI(4,5)P_2. Furthermore, we analyzed the ANTH-ENTH-diC8-PI(4,5)P_2 sample by analytical ultracentrifugation, which also indicated the presence of supramolecular assemblies with an approximate size of 450 kDa (Figure S1B). To characterize the size and composition of the ANTH-ENTH assemblies more precisely, we used native mass spectrometry (Benesch et al., 2007; Heck, 2008). We measured and compared molecular masses of ANTH-ENTH-diC8-PI(4,5)P_2 assemblies made of either untagged or HA-tagged proteins and found that the ANTH domain, the ENTH domain and diC8-PI(4,5)P_2 form an oligomeric complex of 8 ANTH, 8 ENTH, and 22 ± 1 lipid molecules (Figures 1D and S1C).

Based on the observation that the soluble lipid ligand diC8-PI(4,5)P_2 is a part of the ANTH-ENTH oligomeric complex, we

tested whether the PI(4,5)P_2-binding surfaces of ANTH and ENTH domains are required for the complex formation. We therefore repeated the ITC experiments using known ANTH and ENTH PI(4,5)P_2-binding mutant proteins (ANTH KKKH-AAAA; ENTH R62A, H72A) (Ford et al., 2001, 2002). We found that the formation of the oligomeric ANTH-ENTH-diC8-PI(4,5)P_2 complex was disrupted by the ENTH mutation and significantly weakened by the ANTH mutation (Figure S1D). This indicates that PI(4,5)P_2 binding to both ANTH and ENTH molecules is critical for the assembly of the complex. Together, our data show that the ANTH domain of Sla2 and the ENTH domain of Ent1 form a regular oligomeric complex in a PI(4,5)P_2-dependent manner in vitro.

ANTH and ENTH Domains Form a Regular Coat on Membranes In Vitro

The propensity of Sla2's ANTH and Ent1's ENTH domains to oligomerize in a PI(4,5)P_2-dependent manner in solution prompted us to test whether these domains could also oligomerize on their physiological substrate, the lipid bilayer. We therefore incubated both domains with PI(4,5)P_2-containing giant unilamellar vesicles (GUVs) and imaged them with electron cryo-microscopy (cryo-EM). We found that while the ANTH domain alone bound to GUVs sporadically (Figure 2A), the ENTH domain covered them densely and reshaped the GUV membranes into irregular tubules and small vesicles (Figure 2B), in agreement with previous negative staining experiments on liposomes (Ford et al., 2002; Boucrot et al., 2012). Incubation of GUVs with both ANTH and ENTH domains together resulted in a remarkable change of the shape of GUVs into regular membrane tubules with a diameter of 300 to 400 Å. All tubules as well as less abundant flatter areas of membrane appeared to be covered by a regular protein coat (Figure 2C). The regular protein coat on both membrane profiles was clearly shown by 2D class averages (Figures 2D and 2E) and confirmed by Fourier analysis of raw images (Figures 2F and 2G). Moreover, analysis of the tips of the tubules revealed they were also covered by a protein coat (Figure 2H). The ANTH and ENTH domains together can thus form a regular coat on PI(4,5)P_2-containing membranes in vitro.

Structure of ANTH-ENTH Lattice on Membrane Tubules

Class average analysis of the tubules made from GUVs in the presence of both ANTH and ENTH domains showed that the tubules fell into six distinct diameter classes ranging from 300 to 400 Å and exhibited no apparent polarity (Figure 3A). The most abundant class with the diameter of 340 Å contained about 55% of all tubules. This class was used for further structural analysis.

To determine the symmetrical arrangement of the ANTH-ENTH protein coat on membrane tubules, we used electron cryo-tomography and subtomogram averaging (Bharat et al., 2011; Briggs, 2013) (Figure S2). The basic helical turn of the 340 Å diameter tubule is made of approximately ten subunits organized in either one-start or two-start helices with an additional dihedral symmetry perpendicular to the helix axis. We then determined the structures of these one-start and two-start helices at 18.3 Å and 13.6 Å resolution, respectively, using single-particle based helical reconstruction (Desfosses et al., 2014 and Experimental Procedures) (Figures 3B, S2D, S3A, and S3E). The radially averaged cross-section of the 3D reconstruction revealed three strong densities at the 65, 100, and 125 Å radius, representing the inner and outer membrane leaflets and the protein domains (Figures 3C and 3D). The asymmetric unit has a large density lobe that protrudes about 70 Å away from the outer membrane leaflet.

A Quasi-Atomic Model of the Helical ANTH-ENTH Co-assembly

To interpret the organization of the ANTH and ENTH domains on membrane tubules, we built homology models of both domains and fitted them into the EM density. The dimensions of the ANTH domain restricted the fit to the large density lobe distal to the membrane, while the smaller globular density close to the lipid bilayer accommodated the ENTH domain (Figures 4A–4D). The fit positioned the amphipathic "helix 0" of the ENTH domain in the phospholipid head group region of the outer membrane leaflet as previously proposed (Ford et al., 2002; Kweon et al., 2006; Lai et al., 2012; Yoon et al., 2010). The positively charged PI(4,5)P_2-binding patches of the ANTH and ENTH domains (Ford et al., 2001, 2002; Stahelin et al., 2003) face the phospholipid head groups and the negatively charged surface of ANTH is directed away from the membrane (Figure 4E). The PI(4,5)P_2-binding site of the ENTH domain, derived from the homolog crystal structure (Ford et al., 2002), is thus located in the head group region of the bilayer in the EM density (Figures 4B and 4D). Interestingly, the PI(4,5)P_2-binding site of the ANTH domain (Ford et al., 2001) is further away from the head group region (Figures 4B and 4D), suggesting either that it is not occupied by PI(4,5)P_2 in the co-assembly or that the PI(4,5)P_2 ligand is displaced from the head group region of the membrane. In summary, the quasi-atomic model of the ANTH-ENTH co-assembly shows that the ENTH domains are closely attached to the membrane, forming the lipid anchor of the lattice, whereas the ANTH domains are found in a staggered arrangement ~15 Å away from the membrane surface, acting as a structural organizer of the lattice (Figure 4F and Movie S1).

Specific Point Mutations Inhibit the ANTH-ENTH Co-assembly In Vitro

To assess the role of the ANTH-ENTH lattice in endocytosis, we chose a genetic approach and aimed to identify point mutations in the ANTH and ENTH domains, which would specifically inhibit formation of the ANTH-ENTH co-assembly in vitro and to study their impact on endocytic vesicle budding in vivo. We focused on two strongly conserved residues, arginine 29 in ANTH and threonine 104 in ENTH, and mutated them to alanine or glutamate (ANTH R29A, ENTH T104A, ANTH R29E, and ENTH T104E). Both residues reside at the main interface between the ANTH and ENTH domains, which makes up the longitudinal contacts in the tubular ANTH-ENTH lattice (Figure 5A and Movie S1). Notably, the T104A mutation was previously shown to be a loss-of-function mutation in yeast Ent1 and in the homologous epsin in slime mold *Dictyostelium discoideum* (Brady et al., 2010; Wendland et al., 1999). We first tested the effect of ANTH R29 and ENTH T104 mutations on the formation of the oligomeric ANTH-ENTH-diC8-PI(4,5)P_2 complex in solution. We repeated the ITC experiments using either the ANTH R29A or ENTH T104A alanine mutant and detected an approximate 50-fold

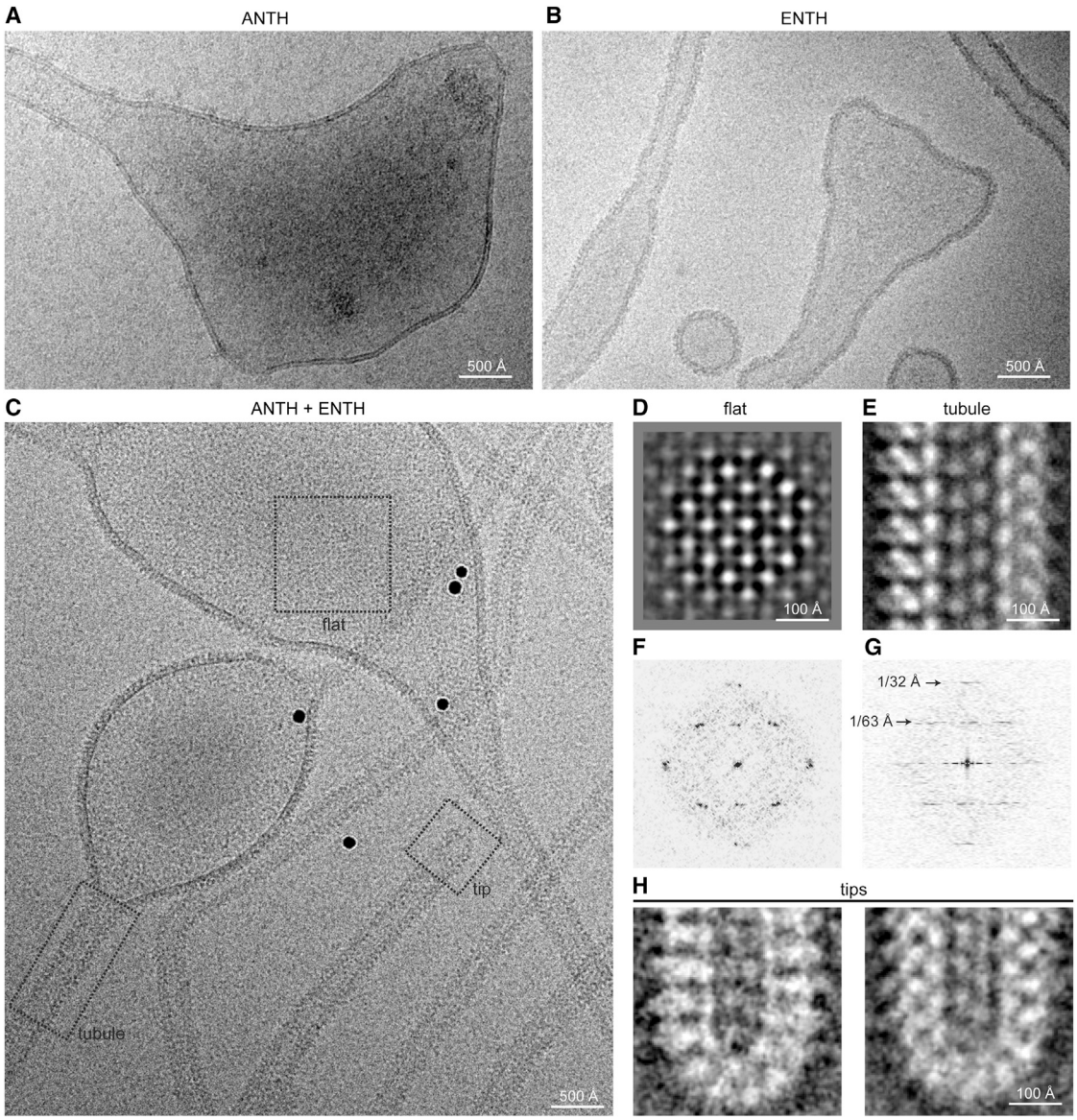

Figure 2. ANTH and ENTH Domains Form a Regular Coat on PI(4,5)P_2-Containing Membranes In Vitro

(A and B) Electron cryo-micrographs of PI(4,5)P_2-containing giant unilamellar vesicles (GUVs) incubated with ANTH (A) and ENTH (B) domain.

(C) Electron cryo-micrograph of PI(4,5)P_2-containing GUVs incubated with ANTH and ENTH domains together. Observable membrane morphologies are indicated by dashed lines: flat membranes, tubules, and tubule tips.

(D and E) 2D class-averages of flat membrane (D) and tubule (E) segments.

(F and G) Rotationally aligned power spectra of segments from flat membrane (F) and tubule (G) from insets of micrograph (C) demonstrate the conservation of lattice parameters on different membranes.

(H) 2D class-averages of tubule tips.

increase of the overall K_d of the ANTH-ENTH-diC8-PI(4,5)P_2 co-assembly. Strikingly, when we measured the complex formation between the ANTH R29E or ENTH T104E glutamate mutant and their wild-type ENTH or ANTH domain partners, no binding could be detected by ITC (Figure 5B). In agreement with the ITC results, regular particles of the ANTH-ENTH-diC8-PI(4,5)P_2 complex could still be observed by negative staining in the case of the alanine mutants, but no particles were detected in the case of the glutamate mutants (Figure 5C). This suggests that the ANTH R29A or ENTH T104A alanine mutants co-assembled into ANTH-ENTH-diC8-PI(4,5)P_2 oligomers with reduced affinity, whereas the ANTH R29E and ENTH T104E glutamate mutants completely failed to oligomerize.

Next, we tested whether the ANTH R29 and ENTH T104 mutants are able to form regularly coated membrane tubules when mixed with their wild-type ENTH and ANTH partners and GUVs. Although all mutant domains bound membranes similarly to the wild-type domains (Figure S5A), they all prevented the

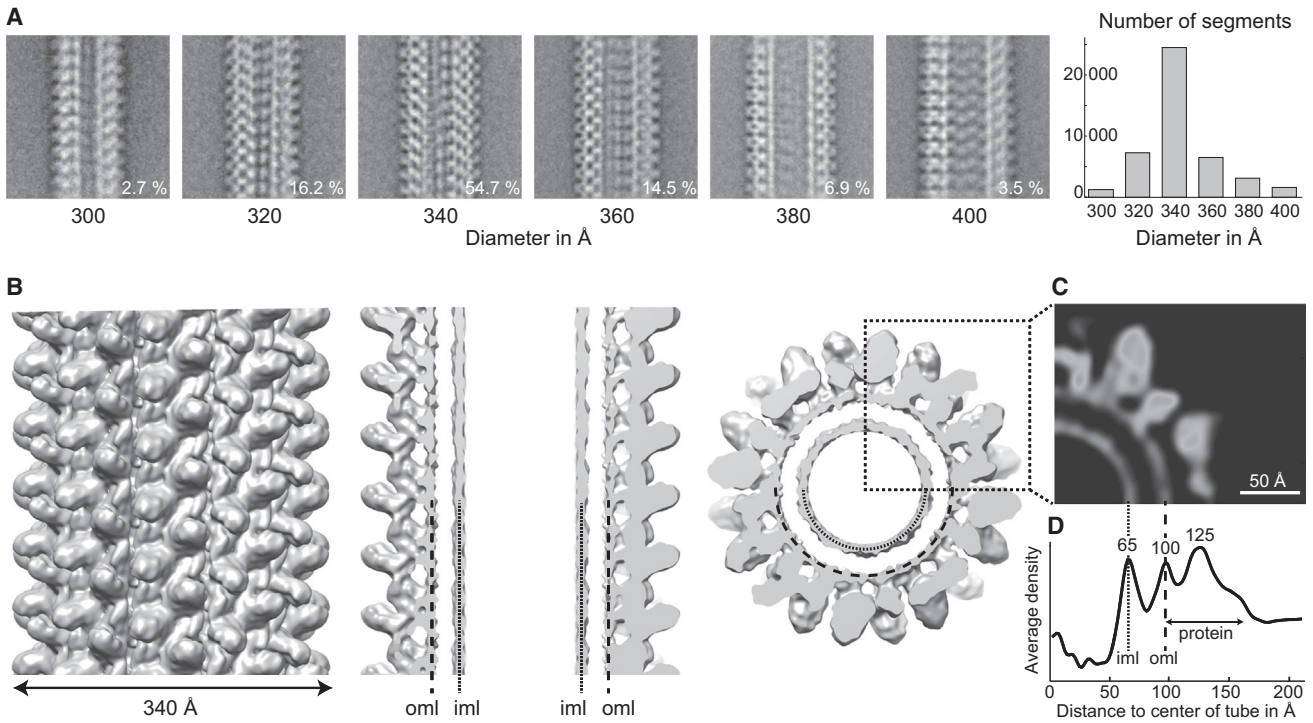

Figure 3. Structure of the ANTH-ENTH-Coated Membrane Tubules

(A) Gallery of representative 2D class-averages of tubule segments for diameters ranging from 300 to 400 Å, respectively (left), together with histogram of diameter distribution (right). The diameter was manually measured on a set of 300 class-averages and assigned to their members.

(B) Isosurface representation of the 3D reconstruction of the two-start, 340 Å diameter tubules at 13.6 Å resolution. The inner (iml) and outer (oml) membrane leaflets are highlighted by dashed lines.

(C) Quarter grayscale slice from cross-sectional density.

(D) Rotationally averaged cross-sectional profile of the 3D reconstruction.

See also Figures S2 and S3.

formation of regularly coated membrane tubules from GUVs (Figure 5D). All mutants gave rise to densely coated irregular tubules (Figure 5D), reminiscent of the tubular profiles observed when GUVs were incubated with the ENTH domain only (Figure 2A). Taken together, the data show that ANTH R29 and ENTH T104 mutations impair the co-assembly of the ANTH and ENTH domains both in solution and on GUV membranes in vitro.

The ANTH-ENTH Co-assembly Is Essential for Endocytosis

To test for the role of the ANTH-ENTH co-assembly in vivo, we introduced the co-assembly-disrupting R29 and T104 point mutations into the Sla2 and Ent1 proteins in yeast. We expressed the mutated copies of *SLA2* and *ENT1* genes under their endogenous promoters in *sla2* and *ent1/ent2* null strains, respectively, and observed their effect on cell growth and endocytosis. Cells expressing Sla2 R29A or Ent1 T104A mutant protein exhibited a mild, temperature-sensitive growth defect, whereas cells expressing Sla2 R29E or Ent1 T104E protein had a strong growth defect (Figure 6A). We analyzed the dynamics of endocytosis in live cells using fluorescent markers for the vesicle coat (Sla1-GFP) and for actin at the endocytic site (Abp1-RFP) (Figure 6B and Movie S2). The appearance of Sla1-GFP at the cell cortex corresponds to the formation of the endocytic coat on a flat plasma membrane. The later appearance of Abp1-RFP and the movement of both Sla1-GFP and Abp1-RFP into the cytoplasm correspond to vesicle budding, which in yeast depends on actin polymerization (Kukulski et al., 2012). In wild-type cells, these endocytic events are highly stereotypic spanning around 25 s between the appearance of Sla1-GFP at the cell cortex and the end of its inward movement (Figures 6B and 6C; Movie S2). In the Sla2 R29A- or Ent1 T104A-expressing cells, the lifetime of Sla1-GFP at the cell cortex was extended (Figure 6C). In addition, in many cases the subsequent inward movement of Sla1-GFP did not occur, suggesting frequent failure of endocytic vesicle budding (Figures 6B and 6C; Movie S2). Cells expressing Sla2 R29E or Ent1 T104E showed an almost complete block of endocytic internalization manifested by stable cortical association of Sla1-GFP during the whole 4-minute time window of imaging (Figures 6B and 6C; Movie S2). Moreover, the arrested Sla1-GFP patches in all mutants were accompanied with dynamic actin tails depicted by Abp1-RFP (see lower kymograph images in Figure 6B and Movie S2). This phenotype indicates that in the co-assembly-disrupting Sla2 R29 and Ent1 T104 mutants, the force of actin polymerization is not properly transmitted to the membrane to drive its invagination, in a similar manner as proposed for *sla2* and *ent1/ent2* null mutant cells (Carroll et al., 2012; Kaksonen et al., 2005; Skruzny et al.,

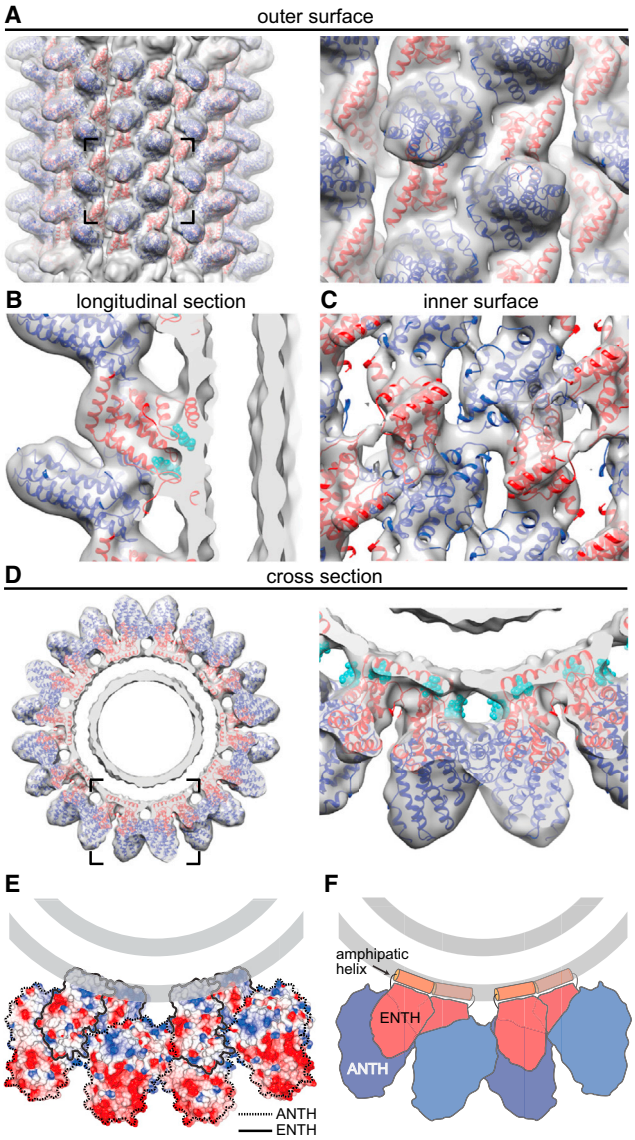

Figure 4. Quasi-Atomic Model of Helical ANTH-ENTH Co-assembly

(A–D) ANTH (blue) and ENTH (red) ribbon models are shown fitted in the cryo-EM map. The atoms of $PI(4,5)P_2$ head groups, represented as cyan spheres in (B and D) are positioned as in the homologous structures. The isosurface contour level σ is 0.5 for (A), (B), and (D) and 1.0 for (C). Right images (A and D) are enlarged views of the areas indicated on the left.

(E) Electrostatic surface representation of the atomic model.

(F) Schematic of the ANTH-ENTH co-assembly structure: ENTH is positioned directly at the membrane with helix 0 immersed into the lipid head groups. By contrast, ANTH is displaced from the membrane with an offset of 15 Å.

The lipid head group regions of the membrane are represented as gray lines in (E) and (F).

See also Figures S2–S4 and Movie S1.

2012). To confirm the endocytic defect of Sla2 R29 and Ent1 T104 strains, we tested the uptake of fluorescent membrane dye FM4-64 by these cells. In all mutant strains, the endocytic uptake of FM4-64 was impaired (Figure S5B). These data strongly suggest that the interaction between the Sla2's ANTH and Ent1's ENTH domains, which is required for their co-assembly into organized protein lattices in vitro, is essential for endocytic vesicle budding in vivo.

Furthermore, we analyzed the effect of co-assembly-disrupting Ent1 T104 mutations on the behavior of Ent1 protein at the endocytic site. Previous studies showed that neither Sla2 nor Ent1 localization to the endocytic site depends on its potential co-assembling partner (Carroll et al., 2012, Newpher et al., 2005; Skruzny et al., 2012). However, recent fluorescence recovery after photobleaching (FRAP) experiments showed that stable binding of Ent1 at the endocytic site is specifically compromised in the absence of Sla2 (Skruzny et al., 2012). To assess if the ANTH-ENTH co-assembly contributes to a stable tethering of Ent1 at the endocytic site, we compared the fluorescence recovery rates of GFP-tagged Ent1 wild-type and GFP-tagged Ent1 T104 mutant proteins (see Supplemental Experimental Procedures for details). We found that both Ent1 T104 mutants localized to endocytic sites but showed significantly faster recovery than wild-type Ent1 protein (Figure 6E), supporting the idea that the ANTH-ENTH co-assembly is critical for the stable association of Ent1 with the endocytic site.

DISCUSSION

Lipid-Triggered Co-assembly of the ANTH and ENTH Domains

Here, we showed that the ANTH domain of Sla2 and the ENTH domain of Ent1 oligomerize into regular co-assemblies in vitro when bound to their lipid ligand $PI(4,5)P_2$. This lipid-triggered ANTH-ENTH co-assembly occurs both in solution with soluble lipid and on the surface of lipid membranes. Based on the cryo-EM structure of the helical ANTH-ENTH lattice on membrane tubules, we identified an interface between the domains that is critical for the co-assembly. The key amino acid residues in this interaction surface are conserved among *Dictyostelium*, yeast, and human and were shown to be essential for the Ent1-Sla2 interaction both in slime mold and yeast (Brady et al., 2010; Skruzny et al., 2012). Notably, recent pull-down experiments performed with homologous mouse proteins (Messa et al., 2014) suggest that the lipid-induced co-assembly activity of the ANTH and ENTH domains is also conserved in mammals. We thus predict that the co-assembly of Sla2 and Ent1 proteins via their ANTH and ENTH domains is evolutionarily conserved in most eukaryotes.

Intact lipid-binding sites of the ANTH and ENTH domains are required for the co-assembly, although both of the binding sites are located away from the ANTH-ENTH interaction surfaces. The mechanism of ANTH-ENTH co-assembly may therefore involve conformational changes induced by lipid binding.

The endocytic coat is assembled from the cytosolic protein pool during each vesicle budding event and then rapidly disassembled. $PI(4,5)P_2$ is required for the early stages of vesicle budding in both yeast and mammals (Zoncu et al., 2007; Sun and Drubin, 2012). $PI(4,5)P_2$-triggered protein-protein interactions could therefore be an efficient way to spatially and temporally regulate the assembly of the coat proteins. We envisage that similar lipid-induced protein-protein interactions could be common in membrane-associated supramolecular structures; e.g., in various membrane trafficking pathways where other lipid-binding adaptor proteins are involved.

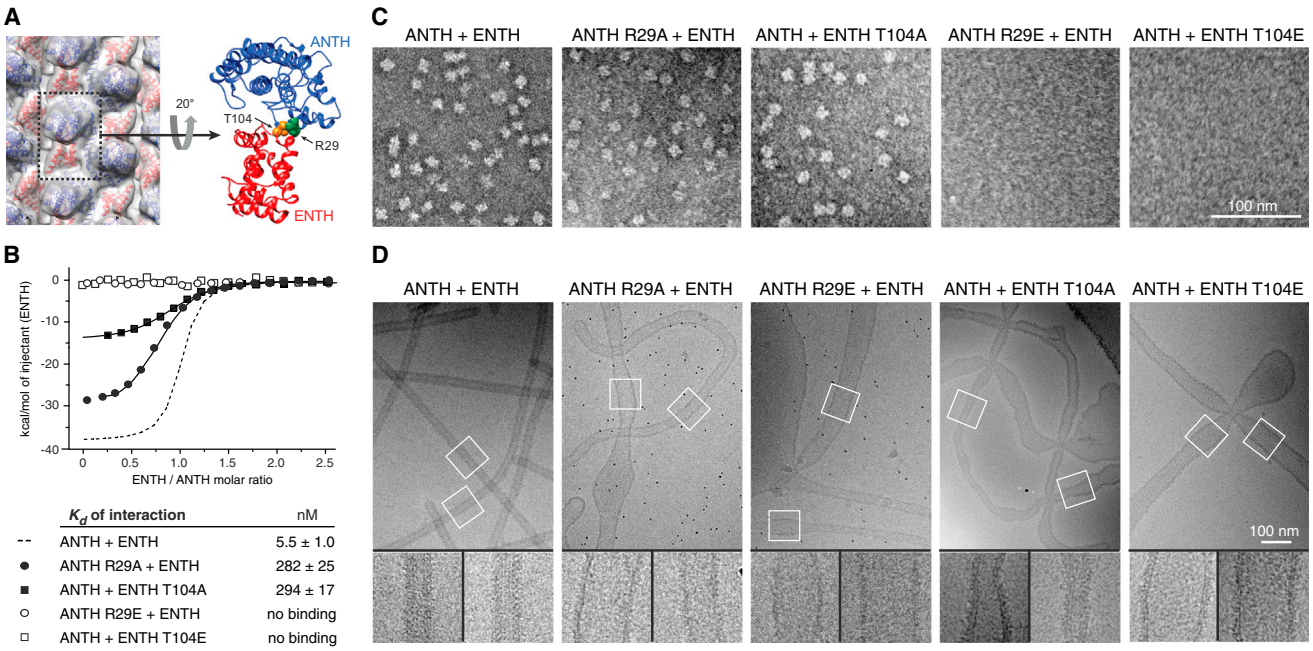

Figure 5. Specific Point Mutations Inhibit the ANTH-ENTH Co-assembly In Vitro

(A) The longitudinal interface of the ANTH-ENTH lattice with ANTH R29 and ENTH T104 residues presented as spheres.

(B and C) ANTH R29 and ENTH T104 mutations impair diC8-PI(4,5)P_2-dependent ANTH-ENTH oligomerization in vitro. The interaction between indicated proteins was analyzed by ITC (B) and negative staining (C). The ANTH-ENTH ITC measurement from Figure 1B is shown for comparison.

(D) ANTH R29 and ENTH T104 mutants are unable to form regularly coated membrane tubules on GUVs when mixed with the wild-type ENTH and ANTH partners, respectively. Insets, 100 × 100 nm.

See also Figure S5 and Movie S1.

The ANTH and ENTH Domains Form a Regular but Flexible Lattice on Membranes

Our cryo-EM studies revealed that the ANTH and ENTH domains co-assemble into regular lattices upon binding to PI(4,5)P_2-containing membranes. Both domains individually bind to PI(4,5)P_2-containing liposomes (Itoh et al., 2001; Ford et al., 2001) and the ENTH domain was shown to tubulate and vesiculate them (Ford et al., 2002; Boucrot et al., 2012). Remarkably, when the two domains were combined, they formed regular lattices on the membrane and induced formation of long and regular membrane tubules. Notably, the tubules covered by the ANTH-ENTH lattice were more regular than those formed by the ENTH domain alone (compare Figures 2B and 2C) and no vesiculation was observed. The ANTH-ENTH lattice formed on membranes of variable curvature, suggesting that the interactions between the domains are adjustable to support different membrane curvatures.

Detailed structural analysis of the ANTH-ENTH lattice revealed that the ENTH domains are more closely associated with the membrane than the ANTH domains. The ENTH domain may therefore function as a membrane anchor, and the ANTH domain as a structural organizer of the lattice. The structural model suggests that the amphipathic helix of the ENTH domain penetrates into the outer membrane leaflet as expected based on earlier structural studies (Ford et al., 2002; Kweon et al., 2006; Lai et al., 2012; Yoon et al., 2010). The amphipathic helix of the ENTH domain has previously been suggested to mediate homomeric interactions between membrane-bound ENTH domains (Yoon et al., 2010; Lai et al., 2012). However, in the ANTH-ENTH lattice the amphipathic helices of the ENTH domains are well aligned and regularly spaced, but not in contact with each other.

Membrane Bending by the ANTH-ENTH Lattice

ENTH domains can bend membranes by inserting an amphipathic helix into the membrane (Ford et al., 2002; Boucrot et al., 2012; Campelo et al., 2008). By contrast, ANTH domains do not have an amphipathic helix, and consequently do not have a significant membrane bending activity (Ford et al., 2002). Our results suggest, however, that an ANTH domain can modulate the membrane bending activity of an ENTH domain. On its own, the membrane bending activity of the ENTH domain results in the formation of tubules and vesicles of variable diameters (Ford et al., 2002; Boucrot et al., 2012; Figure 2B). When the ENTH domains co-assembled with the ANTH domains, we observed only tubules with a restricted range of diameters and no vesiculation (Figures 2C and 5D, left). In the ANTH-ENTH lattice, the amphipathic helices of ENTH domains are organized into an ordered array, which may explain the regular diameter of the formed membrane tubules. In the full-length Sla2 protein, the organizing role of ANTH domains could be further augmented by a dimerization of Sla2 coiled-coil domains and their interaction with the clathrin scaffold. We thus propose that the co-assembly of Ent1 and Sla2 proteins would result in concentrated and uniformly distributed amphipathic helices on the plasma membrane that could contribute to membrane bending at the endocytic site.

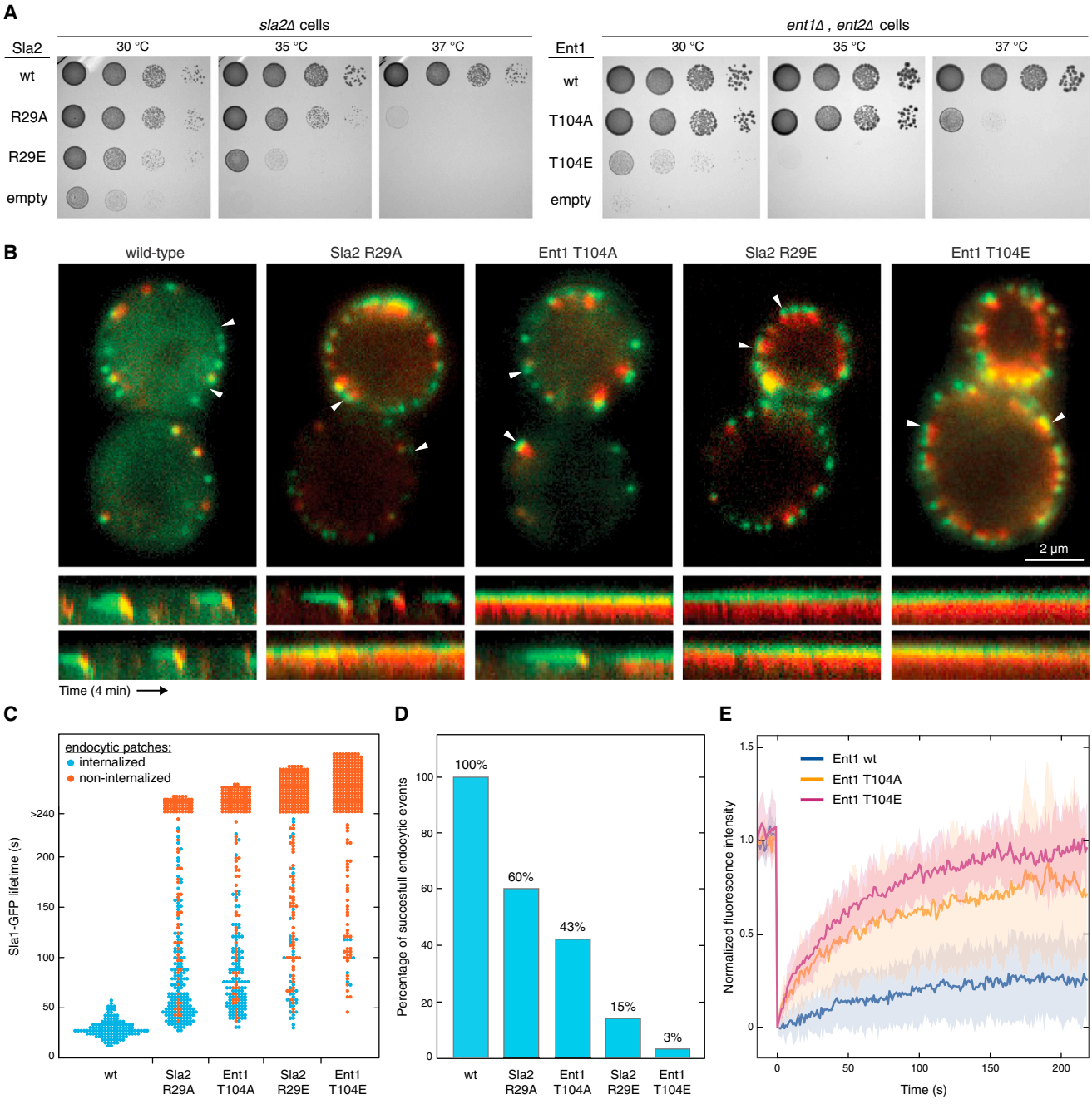

Figure 6. ANTH-ENTH Co-assembly Is Critical for Endocytic Vesicle Budding

(A) Growth defects of Sla2 R29 and Ent1 T104 mutant strains. Ten-fold serial dilutions of *sla2Δ* and *ent1/2Δ* strains expressing indicated proteins were incubated on SC-Ura plates for 1.5–2 days at 30°C, 35°C, and 37°C.

(B) Sla2 R29 and Ent1 T104 mutations cause a strong endocytic defect manifested by arrested endocytic sites (green, coat marker Sla1-GFP) accompanied by polymerizing actin tails (red, actin marker Abp1-RFP). Merged images of wild-type, *sla2Δ* and *ent1/2Δ* strains expressing indicated proteins are shown together with kymographs of selected endocytic patches (arrowheads).

(C) The lifetimes of Sla1-GFP at endocytic patches of strains shown in (B). Internalized and non-internalized (arrested) patches are indicated.

(D) Percentage of successful endocytic events calculated from the number of internalized patches shown in (C).

(E) Fluorescence recovery after photobleaching (FRAP) of Ent1 wild-type and Ent1 T104 mutant proteins in *ent1/2Δ* strain treated with latA. Curves represent the mean ± SD (n = 9–12).

See also Figure S5 and Movie S2.

The ANTH-ENTH co-assembly could also facilitate membrane bending by a scaffolding mechanism, imposing its own curvature on the membrane. However, the ANTH-ENTH lattice was observed both on tubules and on flatter membrane areas indicating that it is flexible enough to accommodate to various membrane curvatures not strongly imposing its own curvature on the membrane.

Additionally, clustering of specific lipid species and protein crowding are other mechanisms suggested to promote membrane bending (Liu et al., 2009; Stachowiak et al., 2012, 2013). By a relatively high affinity of Ent1 to PI(4,5)P_2 and its flexible bulky C terminus, these two mechanisms could potentially have additive effects to the amphipathic helix insertion and scaffolding mechanisms provided by the ANTH-ENTH co-assembly.

Role of the ANTH-ENTH Co-assembly in Endocytosis

Sla2 and Ent1 proteins and their mammalian homologs cooperate to couple actin filaments to the plasma membrane at the endocytic site, and this coupling is critical for vesicle budding (Messa et al., 2014; Skruzny et al., 2012). Using a series of point mutations targeting an ANTH-ENTH interaction surface, we could show that the co-assembly activity of the ANTH and ENTH domains is critical for endocytosis in vivo.

What is the mechanistic role of the ANTH-ENTH co-assembly in endocytosis? During endocytosis, Sla2 and Ent1 arrive among the earliest endocytic proteins (Brach et al., 2014) assembling initially on a flat plasma membrane (Kukulski et al., 2012). Later during vesicle budding, they are located at the tip of the invaginating membrane (Idrissi et al., 2012). We determined the structure of the ANTH-ENTH lattice on the tubular membrane profiles in vitro because they are most amenable for the helical reconstruction approach used. However, the protein coating was also observed on both flat membranes and at the tips of the tubules (Figures 2C–2H), indicating that the ANTH-ENTH lattice could be assembled on these membrane shapes in vivo.

The mutant forms of Sla2 and Ent1 could still localize at the endocytic site, as could the coat-associated protein Sla1, suggesting that the ANTH-ENTH co-assembly is not needed for the initial formation of the endocytic coat. The co-assembly-disrupting mutants inhibited the late actin-dependent vesicle budding step of endocytosis. This phenotype is identical to the phenotypes caused by full deletions of Sla2 or Ent1/2, combined deletions of Sla2's and Ent1's actin binding domains (Kaksonen et al., 2003; Carroll et al., 2012; Skruzny et al., 2012) and notably to the phenotype of PI(4,5)P_2 depletion in yeast (Sun and Drubin, 2012).

We hypothesize that the PI(4,5)P_2-induced ANTH-ENTH co-assembly is critical for efficient transmission of the pulling force from the polymerizing actin cytoskeleton to the plasma membrane. The forces required for membrane invagination in yeast are thought to be in the range of hundreds of picoNewtons (Basu et al., 2014; Carlsson and Bayly, 2014). To exert such a force efficiently, a strong attachment with multiple anchoring sites between the membrane and the endocytic coat is likely to be required (Carlsson and Bayly, 2014). The regular co-assembly of ANTH and ENTH domains could distribute the pulling forces evenly over a larger membrane area thus leading to efficient force transmission and membrane invagination.

Conclusion

We have shown that clathrin adaptor proteins Sla2 and Ent1 can form organized lattices on membranes via their membrane-binding domains. These findings provide a molecular mechanism to the critical interplay of Sla2 and Ent1 proteins and their homologs observed during endocytosis in yeast, *Dictyostelium*, and mouse (Brady et al., 2010, Messa et al., 2014; Skruzny et al., 2012). The formation of the Sla2-Ent1 co-assembly requires both the ANTH and ENTH domains and their lipid ligand PI(4,5)P_2. These findings exemplify an assembly principle that may be common in organizing and regulating membrane-associated protein complexes.

EXPERIMENTAL PROCEDURES

Protein Purification

Recombinant ANTH (amino acids [aa] 1–286) and ENTH (aa 1–154) proteins were purified as 6×His-GST-fusions using Ni-NTA affinity (QIAGEN) and ion exchange HiTrap Q chromatography (GE Healthcare) as described in the Supplemental Experimental Procedures. Circular dichroism experiments showed that all mutated ANTH and ENTH proteins had similar secondary structures and thermal stability as their wild-type counterparts.

Biophysical Characterization of the ANTH-ENTH Interaction

Tris-glycine (pH 7.0) 0.5% agarose native gel electrophoresis was performed with 10–20 μl of protein-lipid mixes containing 0.2–0.4 nmol of purified proteins and 1–2 nmol of diC8-PIP$_2$ (Echelon) incubated in 20 mM HEPES (pH 7.5); 100 mM KCl (ITC buffer) at 25°C for 5–10 min. Samples with 15% glycerol were run at 10 V/cm at 4°C and stained with SimplyBlue SafeStain (Life Technologies).

Binding affinities of wild-type and mutant ANTH and ENTH proteins were determined by ITC using a MicroCal VP-ITC calorimeter (GE Healthcare). Purified proteins were first dialyzed against ITC buffer followed by the adjustments of diC8-PIP$_2$ lipid (Echelon) concentration to 100 μM. Typically, 12 μl injections of 100 μM ENTH protein were performed at 5-min intervals into 10 μM ANTH protein at 25°C. ITC data were corrected for the dilution heat and analyzed using Origin software (version 7.0).

Sedimentation velocity experiments and data analysis were done as described elsewhere (Stuwe et al., 2008) using 10 μM ANTH and ENTH proteins in ITC buffer containing 100 μM diC8-PI(4,5)P_2.

Native Mass Spectrometry

ANTH-ENTH-diC8-PI(4,5)P_2 complexes (with untagged or only ANTH-HA-tagged domains) preassembled at a 1:0.7:3.5 molar ratio were buffer exchanged to 300 mM ammonium acetate (pH 8.0), 1 mM DTT using centrifugal filter units (Sartorius, Vivaspin 500, MWCO 5000). ANTH-ENTH-diC8-PI(4,5)P_2 complex with both domains HA-tagged was exchanged to 100 mM ammonium acetate (pH 7.5), 1 mM DTT. Gold-coated borosilicate capillaries for nano-electrospray ionization were prepared in house (Snijder et al., 2013). Protein complexes (15–30 μM monomer concentration) were analyzed on a modified QToF 1 or 2 (Waters, MS Vision) (van den Heuvel et al., 2006) in positive ion mode using ~1.5×10^{-2} mbar xenon as collision gas (Lorenzen et al., 2007). Collision voltages were varied from 50 V to 200 V. Capillary and sample cone were at 1350 V and 150 V, respectively. Data were analyzed with MassLynx (Waters). Average masses (± SD) were taken from independent experiments (see Figure S1).

Sample Preparation for Electron Microscopy

For preparation of negatively stained samples, protein-lipid mixes (~0.1 mg/ml of protein, 4× molar excess of lipid) were incubated in ITC buffer (see above) at 25°C for 5–10 min and then applied to a carbon-mica interface, stained by floating on a 2% (w/v) uranyl acetate, and transferred to a copper grid. Multiple grids were inspected, and duplicate experiments performed.

GUVs were made by electroformation (Angelova and Dimitrov, 1986). Lipids (76 mol% DOPC, 16 mol% DOPS, 8 mol% porcine brain PI(4,5)P_2; Avanti Polar Lipids) were combined in chloroform:methanol (2:1, v/v) at 10 mg/ml total

concentration and 1% red fluorescent lipidic dye DiI (Invitrogen, D-282) was added. The lipid solution was dried as a thin layer on indium-tin-oxide coated glass slides (Delta Technologies). Two coated slides were assembled with 3 mm silicon spacers to form a chamber, which was filled with 500 mM sucrose. Electroformation was performed overnight applying a 2.5 V, 10 Hz sinusoidal voltage across the chamber. An equal volume of iso-osmolar glucose solution was then added and the GUVs were harvested by overnight sedimentation at 4°C. Ten micromoles ENTH, 10 μM ANTH, or both proteins together were mixed with 2 μl of GUVs in ITC buffer (final volume 40 μl). Following incubation at 25°C for 60 min, 3 μl Protein-A conjugated 10 nm colloidal gold was added as fiducial markers for tomography. The mix was applied to glow discharged C-flat holey carbon coated grids (Protochips) and vitrified by plunge freezing into liquid ethane (Dubochet et al., 1988).

Electron Microscopy

For assessment of morphology from 2D images, cryo-EM was performed on an FEI Tecnai Polara transmission electron microscope equipped with a Gatan GIF 2002 post column energy filter and a 2k × 2k Multiscan charge-coupled device (CCD) camera, operated at 200 kV. Images were collected at 27,500× magnification giving a pixel size of 4.9 Å at the specimen level, with a total estimated dose of 25 $e^-/Å^2$. For structural studies, the vitrified specimens were imaged on an FEI Titan Krios transmission electron microscope operated at 120 kV. Tomographic data were acquired using a Gatan GIF 2002 post column energy filter and a 2k × 2k Multiscan CCD camera. Tilt series were collected with a tilt range of ± 60° with a 3° increment and a total dose of 35 $e^-/Å^2$ at 19,500× magnification, giving a pixel size of 4.3 Å. The defoci varied from −1.5 to −2.5 μm. Images for helical reconstruction were acquired using a US4000 Gatan CCD camera at 59,000× magnification resulting in a final pixel size of 1.78 Å on the specimen. The deposited dose was estimated at 10 $e^-/Å^2$. The defoci varied from −0.5 to −5 μm.

Tomogram Processing and Single-Particle-Based Helical Reconstruction

Tomographic data were processed essentially as described (Bharat et al., 2011; Schur et al., 2013, Zanetti et al., 2013). Briefly, tomogram reconstruction and contrast transfer function correction were performed using the IMOD software (Kremer et al., 1996), whereas subtomogram averaging was done using MATLAB scripts derived from the TOM and AV3 packages (Förster et al., 2005; Nickell et al., 2005). In total, 57 ANTH-ENTH tubules were used for analysis. Using the radius of each tubule as prior information, evenly and arbitrarily distributed positions for subtomogram extraction were assigned on the surface of each tubule. After subtomogram averaging, the positions and orientations of the aligned subtomograms were displayed in 3D space using Amira software (FEI), giving a visual representation of the arrangement of the asymmetric unit cells. All tubules were inspected visually: 33 of them appeared to be two-start helices and 24 of them were one-start helices. All tubules showed a close to an integer number of units per helix turn. The most abundant group of tubules contained 20 two-start helixes with approximately 10 units per helix turn. The width of one complete helix turn (the pitch) was measured using the Euclidean distances between the aligned subtomograms. For a one-start helix the pitch was estimated to be 64 Å, and for the two-start helix, 128 Å. These helical parameters were used as a starting point in symmetry grid search during 2D helical processing (see below).

To assess the regularity of the lattice present on flat or low-curvature membranes, we first examined the power-spectrum of large micrograph areas (over 1,000 × 1,000 Å; Figure 2C). For those areas where power-spectrum intensity peaks indicated regularity, overlapping images of 356 × 356 Å were excised using a step size of approximately 60 Å, yielding a stack of 800 images. Those images were normalized and low-pass filtered to 15 Å, and subjected to five iterations of classification in IMAGIC (van Heel et al., 1996) and alignment in SPIDER (Frank et al., 1996; Shaikh et al., 2008). The resulting class averages (Figure 2D) showed striking resemblance to the tubular lattice (Figure 2E) with alternating stronger and weaker density corresponding to the projection of ANTH and ENTH, respectively. To obtain class averages of the tips (Figure 2H), 988 images of 456 × 456 Å were processed as described above. The resulting 20 classes showed variation in diameter, similar in range to the one observed for the helical segments, with a preferred diameter of 340 Å.

Structure determination of helical tubules was carried out using the image-processing package for single-particle based helical reconstruction SPRING (Desfosses et al., 2014) that is an extended version of the IHRSR procedure (Egelman, 2000). Briefly, the contrast transfer function (CTF) of the micrographs was determined using CTFFIND and a local CTF was further estimated using CTFTILT (Mindell and Grigorieff, 2003). A total of 8,656 tubules were selected using e2helixboxer.py from the EMAN2 suite (Tang et al., 2007). A total of 45,202 segments with dimension 520 × 520 Å were excised using a mean step size of 120 Å, and for classification only an additional random shift along the helix between −60 and 60 Å was added to avoid high-resolution artifacts in the class average power spectra introduced by regularly shifted images. For classification, the segments were further corrected for their CTF by phase flipping, and aligned to the vertical axis. For reconstruction, the segments were CTF-convolved and kept in their original orientation on the micrograph. Two-dimensional (2D) classification of helical segments was performed using SPARX' k-means algorithm (Hohn et al., 2007). The segments were classified and iteratively aligned against a subset of class averages chosen based on their quality with a total of five iterations. We found that the major variability among tubule segments was their diameter, ranging from 300 to 400 Å, and we chose class-averages for each diameter as references for segment alignment in subsequent cycles. Finally, from 300 class-averages the diameter was manually measured. For further processing only segments with a diameter of 340 Å (55% of the segments) and showing helical diffraction beyond the second layer line at 1/35 Å were considered, yielding in a subpopulation of 18,128 segments (40% of the total dataset). Starting from the symmetry estimates of the one-start and two-start helices obtained from electron tomography, we further sorted our segments using multi-model refinement. Thus, we determined two structures of the one-start and two-start helix at a resolution of 21 Å and 16 Å (FSC 0.5 cut-off), respectively. The model or symmetry assignments from this refinement were used to further divide the dataset in two subsets containing 4,286 and 13,842 segments for the one-start and the two-start symmetry, respectively. In order to refine the symmetry parameters, each subset was subjected to symmetry search grid with a pitch ranging from 63 to 64 Å, step 0.1 (one-start), and 126 to 128 Å, step 0.2 (two-start), and for both, units per turn ranging from 9.94 to 10.06 Å, step 0.01 (Figures S3C and S3D). The maximum of the mean cross correlation peak was found at a pitch of 127.2 Å, 10.04 units per turn for the two-start and a pitch 63.2 Å, 9.96 units per turn for the one-start helix. Using the refined symmetry parameters, we performed a high-resolution structure refinement and the resolution improved to 13.6/11.2 Å and 18.3/12.5 Å (FSC 0.5/0.143) for the main two-start and one-start helix reconstruction (Figure S3A). The power spectrum of the 3D reconstruction agrees well with the sum of the power spectra from unaligned segments (Figure S3B). For visual display and the fitting, the EM map of the main two-start reconstruction was filtered to 11 Å and sharpened using a B-factor of $-1{,}000\ 1/Å^2$; the EM map of the one-start helix was filtered to 15 Å and sharpened using a B-factor $-1{,}500\ 1/Å^2$.

Quasi-Atomic Model Building and Refinement

We built homology models of the ANTH and ENTH domains using I-TASSER (Roy et al., 2010) that used Protein Data Bank (PDB) IDs 1hf8 and 1h0a as the main contributing templates with sequence identities of 19% and 46%, respectively. The fitting of these structures into the map of the two-start helix was divided into two steps: initial placement of the starting models into the EM density map was performed using the rigid-body fit feature in UCSF Chimera (Pettersen et al., 2004), after which the structure was allowed to relax into the EM map using deformable elastic network (DEN)-restrained real-space refinement as implemented in DireX (Schröder et al., 2007). In Chimera, 60 random global fit searches in a radius corresponding to the asymmetric unit were followed by local fits resulting in ~20 unique positions for ANTH and ENTH, respectively. We further eliminated fits where the lipid-binding interface was located opposite to the lipid bilayer in the 3D reconstruction, resulting in a total of three and five plausible solutions for ANTH and ENTH, respectively. Furthermore, we created eight symmetry-related copies of the ANTH-ENTH heterodimer to simulate the interfaces between asymmetric units in the helical lattice and applied Chimera's sequential fit procedure for each of the 15 combinations in an iterative manner until the solutions converged. As a result, only a single unique orientation of the ANTH-ENTH

heterodimer was found that was encompassed well by the EM envelope. Prior to flexible fitting, this structure was energy-minimized in PHENIX (Adams et al., 2010) to resolve steric clashes in the dimer interface. The structure was then further refined using 500 steps of DireX refinement. We performed a grid search over several refinement parameters (den_strength, den_gamma, pert_fac) to identify solutions that optimally balance map correlation and deviation from the reference structures. To avoid over-fitting we limited the map resolution to 12 Å and included additional secondary structure restraints from the reference structures. The parameter search was evaluated by the highest map correlation while eliminating physically improbable solutions in terms of stereochemistry and clash scores. We found minimal RMSD from the well-conserved ENTH domain as a consistent readout that our fitting restraints were sufficiently conservative/strong to prevent over-interpretation of the density map. Finally, for our selected model, we applied the parameter values 0.02, 0.6, and 0.05 for pert_fact, den_strength, and den_gamma. We observed convergence to similar solutions for other parameter combinations. A final energy minimization step with weak restraints on the main chain atoms was performed to resolve geometry imperfections arising from the DireX refinement. As a result of the DireX refinement, the model showed noticeable improvement in the fit of helix 0 and 8 of ENTH and the fit of the C-terminal helices of ANTH (Figure S4). We determined the RMSD of ANTH and ENTH with respect to the unrefined models at 3.4 and 2.3 Å, respectively, which reflects the higher sequence conservation of ENTH. Finally, we computed the FSC between the original and a simulated map from refined model coordinates to which helical symmetry was applied. The resulting FSC cut-off values at 13.3/10.1 (FSC 0.5/0.143) are very similar when compared with the original FSC computed from half datasets (Figure S3A).

Liposome Flotation Assays

Liposomes consisting of 96 mol% DOPC and 4 mol% PI(4,5)P_2 (for assays with ENTH proteins) or 76 mol% DOPC, 16 mol% DOPS and 8 mol% PI(4,5)P_2 (for assays with ANTH proteins) (Avanti Polar Lipids) were prepared and assays performed as described elsewhere (Skruzny et al., 2012). Binding of mutant proteins was calculated as a percentage of binding of wild-type protein (100% binding) and shown as an average ± SD from three independent assays.

Live-Cell Imaging

Yeast strains were generated by homologous recombination with PCR cassettes (Janke et al., 2004) and crossing. Live-cell imaging and FRAP experiments were performed using an Olympus IX81 microscope with 100×/NA 1.45 PlanApo objective and cells grown in SD medium at 25°C. The acquired image series were processed and analyzed in ImageJ. Please see the Supplemental Experimental Procedures for details.

ACCESSION NUMBERS

The Electron Microscopy Data Bank accession numbers for the EM maps of helical tubules are EMD-2896 (two-start helix) and EMD-2897 (one-start helix). The Protein Data Bank accession number for the corresponding fitted coordinates of the ANTH-ENTH helical array on the two-start tubule is PDB: 5avh.

SUPPLEMENTAL INFORMATION

Supplemental Information includes Supplemental Experimental Procedures, five figures, and two movies and can be found with this article online at http://dx.doi.org/10.1016/j.devcel.2015.02.023.

AUTHOR CONTRIBUTIONS

M.S., A.D., S.P., S.O.D., A.G., C.U., A.J.J., M.A., W.J.H.H., J.S., R.M., V.R., and C.S. performed the experiments and analyzed data. M.S. performed biochemical and cell biology experiments, and A.D. acquired and analyzed electron microscopy data. M.S., A.D., C.U., J.A.G.B., C.S., and M.K. designed the study and wrote the manuscript. All authors discussed the results and commented on the manuscript.

ACKNOWLEDGMENTS

We thank S. Rybina and the EMBL Protein Expression and Purification Facility for the recombinant proteins. We acknowledge support of high-performance computing by Michael Wahlers and Andres Lindau (EMBL IT Services). All mass spectrometry experiments were performed in the lab of A.J.R. Heck at Utrecht University, the Netherlands. M.S. and C.U. were funded by Marie Curie PIEF-GA-2009-237727 and EMBO ALTF 1531-2010 fellowships, respectively. Work in the J.A.G.B. laboratory by S.P. and S.O.D was partially supported by a grant from the Deutsche Forschungsgemeinschaft within SFB 638. A.D., A.G., and A.J.J. were supported by EMBL Interdisciplinary Postdoc (EIPOD) fellowships under Marie Curie Actions (PCOFUND-GA-2008-229597).

Received: October 22, 2014
Revised: November 29, 2014
Accepted: February 25, 2015
Published: April 20, 2015

REFERENCES

Adams, P.D., Afonine, P.V., Bunkóczi, G., Chen, V.B., Davis, I.W., Echols, N., Headd, J.J., Hung, L.W., Kapral, G.J., Grosse-Kunstleve, R.W., et al. (2010). PHENIX: a comprehensive Python-based system for macromolecular structure solution. Acta Crystallogr. D Biol. Crystallogr. *66*, 213–221.

Aghamohammadzadeh, S., and Ayscough, K.R. (2009). Differential requirements for actin during yeast and mammalian endocytosis. Nat. Cell Biol. *11*, 1039–1042.

Angelova, M.I., and Dimitrov, D.S. (1986). Liposome electroformation. Faraday Discuss. Chem. Soc. *81*, 303–311.

Basu, R., Munteanu, E.L., and Chang, F. (2014). Role of turgor pressure in endocytosis in fission yeast. Mol. Biol. Cell *25*, 679–687.

Benesch, J.L., Ruotolo, B.T., Simmons, D.A., and Robinson, C.V. (2007). Protein complexes in the gas phase: technology for structural genomics and proteomics. Chem. Rev. *107*, 3544–3567.

Bharat, T.A., Riches, J.D., Kolesnikova, L., Welsch, S., Krähling, V., Davey, N., Parsy, M.L., Becker, S., and Briggs, J.A. (2011). Cryo-electron tomography of Marburg virus particles and their morphogenesis within infected cells. PLoS Biol. *9*, e1001196.

Boucrot, E., Pick, A., Çamdere, G., Liska, N., Evergren, E., McMahon, H.T., and Kozlov, M.M. (2012). Membrane fission is promoted by insertion of amphipathic helices and is restricted by crescent BAR domains. Cell *149*, 124–136.

Boulant, S., Kural, C., Zeeh, J.C., Ubelmann, F., and Kirchhausen, T. (2011). Actin dynamics counteract membrane tension during clathrin-mediated endocytosis. Nat. Cell Biol. *13*, 1124–1131.

Brach, T., Godlee, C., Moeller-Hansen, I., Boeke, D., and Kaksonen, M. (2014). The initiation of clathrin-mediated endocytosis is mechanistically highly flexible. Curr. Biol. *24*, 548–554.

Brady, R.J., Damer, C.K., Heuser, J.E., and O'Halloran, T.J. (2010). Regulation of Hip1r by epsin controls the temporal and spatial coupling of actin filaments to clathrin-coated pits. J. Cell Sci. *123*, 3652–3661.

Brett, T.J., Legendre-Guillemin, V., McPherson, P.S., and Fremont, D.H. (2006). Structural definition of the F-actin-binding THATCH domain from HIP1R. Nat. Struct. Mol. Biol. *13*, 121–130.

Briggs, J.A. (2013). Structural biology in situ—the potential of subtomogram averaging. Curr. Opin. Struct. Biol. *23*, 261–267.

Campelo, F., McMahon, H.T., and Kozlov, M.M. (2008). The hydrophobic insertion mechanism of membrane curvature generation by proteins. Biophys. J. *95*, 2325–2339.

Carlsson, A.E., and Bayly, P.V. (2014). Force generation by endocytic actin patches in budding yeast. Biophys. J. *106*, 1596–1606.

Carroll, S.Y., Stimpson, H.E., Weinberg, J., Toret, C.P., Sun, Y., and Drubin, D.G. (2012). Analysis of yeast endocytic site formation and maturation through a regulatory transition point. Mol. Biol. Cell *23*, 657–668.

Desfosses, A., Ciuffa, R., Gutsche, I., and Sachse, C. (2014). SPRING - an image processing package for single-particle based helical reconstruction from electron cryomicrographs. J. Struct. Biol. *185*, 15–26.

Dubochet, J., Adrian, M., Chang, J.J., Homo, J.C., Lepault, J., McDowall, A.W., and Schultz, P. (1988). Cryo-electron microscopy of vitrified specimens. Q. Rev. Biophys. *21*, 129–228.

Egelman, E.H. (2000). A robust algorithm for the reconstruction of helical filaments using single-particle methods. Ultramicroscopy *85*, 225–234.

Ford, M.G., Pearse, B.M., Higgins, M.K., Vallis, Y., Owen, D.J., Gibson, A., Hopkins, C.R., Evans, P.R., and McMahon, H.T. (2001). Simultaneous binding of PtdIns(4,5)P_2 and clathrin by AP180 in the nucleation of clathrin lattices on membranes. Science *291*, 1051–1055.

Ford, M.G.J., Mills, I.G., Peter, B.J., Vallis, Y., Praefcke, G.J., Evans, P.R., and McMahon, H.T. (2002). Curvature of clathrin-coated pits driven by epsin. Nature *419*, 361–366.

Förster, F., Medalia, O., Zauberman, N., Baumeister, W., and Fass, D. (2005). Retrovirus envelope protein complex structure in situ studied by cryo-electron tomography. Proc. Natl. Acad. Sci. USA *102*, 4729–4734.

Frank, J., Radermacher, M., Penczek, P., Zhu, J., Li, Y., Ladjadj, M., and Leith, A. (1996). SPIDER and WEB: processing and visualization of images in 3D electron microscopy and related fields. J. Struct. Biol. *116*, 190–199.

Heck, A.J. (2008). Native mass spectrometry: a bridge between interactomics and structural biology. Nat. Methods *5*, 927–933.

Henne, W.M., Boucrot, E., Meinecke, M., Evergren, E., Vallis, Y., Mittal, R., and McMahon, H.T. (2010). FCHo proteins are nucleators of clathrin-mediated endocytosis. Science *328*, 1281–1284.

Hohn, M., Tang, G., Goodyear, G., Baldwin, P.R., Huang, Z., Penczek, P.A., Yang, C., Glaeser, R.M., Adams, P.D., and Ludtke, S.J. (2007). SPARX, a new environment for Cryo-EM image processing. J. Struct. Biol. *157*, 47–55.

Idrissi, F.Z., Blasco, A., Espinal, A., and Geli, M.I. (2012). Ultrastructural dynamics of proteins involved in endocytic budding. Proc. Natl. Acad. Sci. USA *109*, E2587–E2594.

Itoh, T., Koshiba, S., Kigawa, T., Kikuchi, A., Yokoyama, S., and Takenawa, T. (2001). Role of the ENTH domain in phosphatidylinositol-4,5-bisphosphate binding and endocytosis. Science *291*, 1047–1051.

Janke, C., Magiera, M.M., Rathfelder, N., Taxis, C., Reber, S., Maekawa, H., Moreno-Borchart, A., Doenges, G., Schwob, E., Schiebel, E., and Knop, M. (2004). A versatile toolbox for PCR-based tagging of yeast genes: new fluorescent proteins, more markers and promoter substitution cassettes. Yeast *21*, 947–962.

Kaksonen, M., Sun, Y., and Drubin, D.G. (2003). A pathway for association of receptors, adaptors, and actin during endocytic internalization. Cell *115*, 475–487.

Kaksonen, M., Toret, C.P., and Drubin, D.G. (2005). A modular design for the clathrin- and actin-mediated endocytosis machinery. Cell *123*, 305–320.

Kirchhausen, T., Owen, D., and Harrison, S.C. (2014). Molecular structure, function, and dynamics of clathrin-mediated membrane traffic. Cold Spring Harb. Perspect. Biol. *6*, a016725.

Kozlov, M.M., Campelo, F., Liska, N., Chernomordik, L.V., Marrink, S.J., and McMahon, H.T. (2014). Mechanisms shaping cell membranes. Curr. Opin. Cell Biol. *29*, 53–60.

Kremer, J.R., Mastronarde, D.N., and McIntosh, J.R. (1996). Computer visualization of three-dimensional image data using IMOD. J. Struct. Biol. *116*, 71–76.

Kukulski, W., Schorb, M., Kaksonen, M., and Briggs, J.A. (2012). Plasma membrane reshaping during endocytosis is revealed by time-resolved electron tomography. Cell *150*, 508–520.

Kweon, D.H., Shin, Y.K., Shin, J.Y., Lee, J.H., Lee, J.B., Seo, J.H., and Kim, Y.S. (2006). Membrane topology of helix 0 of the Epsin N-terminal homology domain. Mol. Cells *21*, 428–435.

Lai, C.L., Jao, C.C., Lyman, E., Gallop, J.L., Peter, B.J., McMahon, H.T., Langen, R., and Voth, G.A. (2012). Membrane binding and self-association of the epsin N-terminal homology domain. J. Mol. Biol. *423*, 800–817.

Liu, J., Sun, Y., Drubin, D.G., and Oster, G.F. (2009). The mechanochemistry of endocytosis. PLoS Biol. *7*, e1000204.

Lorenzen, K., Versluis, C., van Duijn, E., van den Heuvel, R.H.H., and Heck, A.J.R. (2007). Optimizing macromolecular tandem mass spectrometry of large non-covalent complexes using heavy collision gases. Int. J. Mass *268* (Spec.), 198–206.

McMahon, H.T., and Boucrot, E. (2011). Molecular mechanism and physiological functions of clathrin-mediated endocytosis. Nat. Rev. Mol. Cell Biol. *12*, 517–533.

Messa, M., Fernández-Busnadiego, R., Sun, E.W., Chen, H., Czapla, H., Wrasman, K., Wu, Y., Ko, G., Ross, T., Wendland, B., and De Camilli, P. (2014). Epsin deficiency impairs endocytosis by stalling the actin-dependent invagination of endocytic clathrin-coated pits. eLife *3*, e03311.

Mim, C., and Unger, V.M. (2012). Membrane curvature and its generation by BAR proteins. Trends Biochem. Sci. *37*, 526–533.

Mindell, J.A., and Grigorieff, N. (2003). Accurate determination of local defocus and specimen tilt in electron microscopy. J. Struct. Biol. *142*, 334–347.

Newpher, T.M., Smith, R.P., Lemmon, V., and Lemmon, S.K. (2005). In vivo dynamics of clathrin and its adaptor-dependent recruitment to the actin-based endocytic machinery in yeast. Dev. Cell *9*, 87–98.

Nickell, S., Förster, F., Linaroudis, A., Net, W.D., Beck, F., Hegerl, R., Baumeister, W., and Plitzko, J.M. (2005). TOM software toolbox: acquisition and analysis for electron tomography. J. Struct. Biol. *149*, 227–234.

Owen, D.J., Collins, B.M., and Evans, P.R. (2004). Adaptors for clathrin coats: structure and function. Annu. Rev. Cell Dev. Biol. *20*, 153–191.

Pettersen, E.F., Goddard, T.D., Huang, C.C., Couch, G.S., Greenblatt, D.M., Meng, E.C., and Ferrin, T.E. (2004). UCSF Chimera—a visualization system for exploratory research and analysis. J. Comput. Chem. *25*, 1605–1612.

Roy, A., Kucukural, A., and Zhang, Y. (2010). I-TASSER: a unified platform for automated protein structure and function prediction. Nat. Protoc. *5*, 725–738.

Schröder, G.F., Brunger, A.T., and Levitt, M. (2007). Combining efficient conformational sampling with a deformable elastic network model facilitates structure refinement at low resolution. Structure *15*, 1630–1641.

Schur, F.K., Hagen, W.J., de Marco, A., and Briggs, J.A. (2013). Determination of protein structure at 8.5Å resolution using cryo-electron tomography and sub-tomogram averaging. J. Struct. Biol. *184*, 394–400.

Shaikh, T.R., Gao, H., Baxter, W.T., Asturias, F.J., Boisset, N., Leith, A., and Frank, J. (2008). SPIDER image processing for single-particle reconstruction of biological macromolecules from electron micrographs. Nat. Protoc. *3*, 1941–1974.

Skruzny, M., Brach, T., Ciuffa, R., Rybina, S., Wachsmuth, M., and Kaksonen, M. (2012). Molecular basis for coupling the plasma membrane to the actin cytoskeleton during clathrin-mediated endocytosis. Proc. Natl. Acad. Sci. USA *109*, E2533–E2542.

Snijder, J., Uetrecht, C., Rose, R.J., Sanchez-Eugenia, R., Marti, G.A., Agirre, J., Guérin, D.M., Wuite, G.J., Heck, A.J., and Roos, W.H. (2013). Probing the biophysical interplay between a viral genome and its capsid. Nat. Chem. *5*, 502–509.

Stachowiak, J.C., Schmid, E.M., Ryan, C.J., Ann, H.S., Sasaki, D.Y., Sherman, M.B., Geissler, P.L., Fletcher, D.A., and Hayden, C.C. (2012). Membrane bending by protein-protein crowding. Nat. Cell Biol. *14*, 944–949.

Stachowiak, J.C., Brodsky, F.M., and Miller, E.A. (2013). A cost-benefit analysis of the physical mechanisms of membrane curvature. Nat. Cell Biol. *15*, 1019–1027.

Stahelin, R.V., Long, F., Peter, B.J., Murray, D., De Camilli, P., McMahon, H.T., and Cho, W. (2003). Contrasting membrane interaction mechanisms of AP180 N-terminal homology (ANTH) and epsin N-terminal homology (ENTH) domains. J. Biol. Chem. *278*, 28993–28999.

Stuwe, T., Hothorn, M., Lejeune, E., Rybin, V., Bortfeld, M., Scheffzek, K., and Ladurner, A.G. (2008). The FACT Spt16 "peptidase" domain is a histone H3-H4 binding module. Proc. Natl. Acad. Sci. USA *105*, 8884–8889.

Sun, Y., and Drubin, D.G. (2012). The functions of anionic phospholipids during clathrin-mediated endocytosis site initiation and vesicle formation. J. Cell Sci. *125*, 6157–6165.

Tang, G., Peng, L., Baldwin, P.R., Mann, D.S., Jiang, W., Rees, I., and Ludtke, S.J. (2007). EMAN2: an extensible image processing suite for electron microscopy. J. Struct. Biol. *157*, 38–46.

van den Heuvel, R.H.H., van Duijn, E., Mazon, H., Synowsky, S.A., Lorenzen, K., Versluis, C., Brouns, S.J., Langridge, D., van der Oost, J., Hoyes, J., and Heck, A.J. (2006). Improving the performance of a quadrupole time-of-flight instrument for macromolecular mass spectrometry. Anal. Chem. *78*, 7473–7483.

van Heel, M., Harauz, G., Orlova, E.V., Schmidt, R., and Schatz, M. (1996). A new generation of the IMAGIC image processing system. J. Struct. Biol. *116*, 17–24.

Wendland, B., Steece, K.E., and Emr, S.D. (1999). Yeast epsins contain an essential N-terminal ENTH domain, bind clathrin and are required for endocytosis. EMBO J. *18*, 4383–4393.

Yoon, Y., Tong, J., Lee, P.J., Albanese, A., Bhardwaj, N., Källberg, M., Digman, M.A., Lu, H., Gratton, E., Shin, Y.K., and Cho, W. (2010). Molecular basis of the potent membrane-remodeling activity of the epsin 1 N-terminal homology domain. J. Biol. Chem. *285*, 531–540.

Zanetti, G., Prinz, S., Daum, S., Meister, A., Schekman, R., Bacia, K., and Briggs, J.A. (2013). The structure of the COPII transport-vesicle coat assembled on membranes. eLife *2*, e00951.

Zoncu, R., Perera, R.M., Sebastian, R., Nakatsu, F., Chen, H., Balla, T., Ayala, G., Toomre, D., and De Camilli, P.V. (2007). Loss of endocytic clathrin-coated pits upon acute depletion of phosphatidylinositol 4,5-bisphosphate. Proc. Natl. Acad. Sci. USA *104*, 3793–3798.